NANO · MICRO small
www.small-journal.com

High-Performance Lithium-Ion Capacitors Based on Porosity-Regulated Zirconium Metal–Organic Frameworks

Wen Yan, Jian Su, Zhi-Mei Yang, Sen Lv, Zhong Jin, and Jing-Lin Zuo**

Comprised of a battery anode and a supercapacitor cathode, hybrid lithium-ion capacitors (HLICs) are found to be an effective solution to realize both high power density and high energy density at the same time. Organic–inorganic hybrid materials with well-organized framework guided by the reticular chemistry are one of the promising anode materials for HLICs because of rich active sites and ordered porosity. Herein, metal–organic framework consisting of Zr^{4+} metal ions and tetrathiafulvalene-based ligands (Zr-MOF) is proposed as the pseudocapacitive anode of HLICs. The Zr-MOF possesses high stability, high crystallinity, and multiple meso-microporous channels favorable for ion transport. The as-prepared Zr-MOF||activated carbon HLICs present high energy density (122.5 Wh kg^{-1}), high power density (12.5 kW kg^{-1}), and stable cycling performance (86% capacity retention after 1000 cycles at 2000 mA g^{-1}) within the operating voltage range of 1.0–4.0 V. The results expand the direct application of MOF for bridging the performance gap between batteries and supercapacitors.

1. Introduction

With the booming exploitation and utilization of clean and sustainable energy sources, such as wind and solar energy, advanced technologies associated with energy conversion and storage are urgently needed. Although breakthroughs have been achieved in lithium-ion batteries (LIBs, energy density close to 200 Wh kg^{-1}) and electrochemical capacitors (ECs, powder density up to 10 kW kg^{-1}),[1–3] energy-storage devices with both battery-level energy density and capacitor-level high power density are highly desired. It is crucial to intelligently combine the working mechanism of LIBs and ECs simultaneously within one device in which the characteristic advantages can be well remained. The above-mentioned devices, hybrid lithium-ion capacitors (HLICs), consist of a batter-type anode with reversible Li^+ ion insertion/extraction behavior which provides high energy density and a capacitor-type cathode with reversible adsorption/desorption process which ensures high power density.[4,5] However, the electrochemical kinetics based on the ion adsorption/desorption at the cathode side is faster than that of the lithiation/delithiation kinetics at the anode side. In this scenario, the performances of HLICs including power density and cycling stability are severely limited.[6,7] Therefore, the rational design and fabrication of high-performance anode materials with fast kinetics are urgently required.

To overcome the problem of kinetics mismatch, a promising strategy is exploiting pseudocapacitive anode materials that possess fast and reversible redox characteristics.[8] In the reported pseudocapacitive inorganic materials, two main mechanisms of charge storage are proposed: surface redox pseudocapacitance (such as $RuO_2{\cdot}xH_2O$[9] and MnO_2[10]) and intercalation pseudocapacitance (such as T-Nb_2O_5[11] and TiO_2[12]). Notably, the poor surface area and the inappropriate voltage plateau of inorganic metal oxides[9–12] negatively affect the energy density and the operating voltage range of HLICs. Moreover, the lack of designability and functionality restricts further improvement of these anode materials. It is well known that organic molecules can be designed on purpose and the functionalities can be easily modified at atom level. And, some organic polymers including polypyrrole,[13] polyaniline,[14] poly(3,4-ethylenedioxythiophene),[15] polyacetylene,[16] and others,[17,18] also exhibit pseudocapacitive behavior. However, the poor surface area, low capacity, and unstability of these organic polymers[14,17,19] deeply restrict their application in HLICs. Hence, the combination of solid inorganic components with electro-active organic linkers will lead a promising way to obtain suitable anode materials.

Reticular chemistry[20–22] guaranteed metal–organic frameworks (MOFs) with ordered crystallinity and porosity can be a suitable choice for the application of anode materials.[18,23–27] In recent years, great efforts have been made to improve the electron conductivity of MOFs.[28–31] However, the use of poor electron-conducting MOFs in energy storage fields is very limited so far.[32,33] Considering the dominant insulating property of MOFs, exploring their applications in energy storage devices has always been neglected and needs to be valued. Specifically, MOFs with redox-active metal or organic centers/guests that can undergo faradaic redox reactions are potential candidates for the pseudocapacitive materials.[34–38] The lifetimes of the capacitors are inevitably compromised by limited cycling

W. Yan, Dr. J. Su, Z.-M. Yang, S. Lv, Prof. Z. Jin, Prof. J.-L. Zuo
State Key Laboratory of Coordination Chemistry
Collaborative Innovation Center of Advanced Microstructures
Key Laboratory of Mesoscopic Chemistry of MOE
School of Chemistry and Chemical Engineering
Nanjing University
Nanjing, Jiangsu 210023, China
E-mail: zhongjin@nju.edu.cn; zuojl@nju.edu.cn

The ORCID identification number(s) for the author(s) of this article can be found under https://doi.org/10.1002/smll.202005209.

DOI: 10.1002/smll.202005209

stability of pseudocapacitive materials because of their structure disintegration and active material dissolution.[39] Therefore, exploring long-term cycling of electrode materials is crucial for durable and reliable HLICs. Zr-MOFs with robust Zr_6 clusters as metal anodes possess stable 3D framework, which is conducive to the charging/discharging stabilities. Additionally, it is more feasible to modify the pores and ligands of Zr-MOFs than other MOFs. For example, various of ligands with the same lengths can be installed in the Zr_6-MOF to adjust the pore microenvironments.[40] Also, confined growing of pseudocapacitive and conductive organic polymers via an in situ method can be realized to improve the conductivity and electrochemical properties of Zr_6-MOF.[41] Considering the chemical stability and functionality of expected MOFs, Zr-MOFs with strong Zr—O bonds have shown the possibility to act as a service platform to handle with desired applications.[22,42–46] In fact, studies on the redox activity on the electrochemical properties of pristine MOFs remain largely unexplored, especially in the field of HLICs.[3,47–49]

In this report, we investigated the electrochemical properties of three stable and redox-active MOFs consisting of Zr^{4+} metal ions and tetrathiafulvalene-base ligands. Through systematic electrochemical characterizations, we found that high crystallinity and hierarchical nanoporous characteristic of the Zr-MOFs can effectively facilitate the diffusion of Li^+ ions during charge/discharge processes, thus ensuring excellent electrochemical kinetics of the anodes. HLICs employing stable Zr-MOF-1 with hierarchical porosity as anode material and activated carbon (AC) as cathode material exhibit outstanding performances. By utilizing these electrode materials, the well-equipped Zr-MOF-1||AC HLICs show high energy density (122.5 Wh kg^{-1}) and large power density (12.5 kW kg^{-1}) within the operating voltage range of 1.0–4.0 V. To the best of our knowledge, the pristine Zr-MOFs-based electrode possessing pseudocapacitance has not been explored in HLICs. Hence, this work lights the way of applying stable MOFs with poor electron conductivity but amazing pseudocapacitance in energy storage systems.

2. Results and Discussion

The synthesis of Zr-MOF-1 and Zr-MOF-2 was conducted according to our previous work.[50] Zr-MOF-1 was assembled from a six-connected $[Zr_6O_4(OH)_4(PhCOO)_6(COO)_6]$ node and a functional ligand, Me-TTFTB^{4-} (Me-TTFTB = tetrathiafulvalene-tetramethylbenzoate). Zr-MOF-2 and Zr-MOF-3 were constructed by the famous ligand, TTFTB^{4-} (TTFTB = tetrathiafulvalene-tetrabenzoate),[51] and eight-connected $[Zr_6O_8(OH_2)_8(COO)_8]$ node or Zr^{4+} ions, respectively. Notably, the intentional synthesis of Zr-MOF-1 and Zr-MOF-2 can be achieved simply by the topologically guided steric tuning strategy. Moreover, guided by the reticular chemistry, the topology of Zr-MOF-1 and Zr-MOF-2 is predicted in the limited topology of Zr-tetracarboxylate-based MOFs.[42] Specifically, Zr-MOF-1 exhibits two different square channels with the size of 12.4 Å (pink balls) and 21.8 Å (blue balls) (**Figure 1**a), respectively. In the crystallographic ***c*** direction of Zr-MOF-2, the maximum diagonal distance of the aperture sizes for the rhomboid topological channels is ≈15 Å × 33 Å (Figure 1b). The calculations based on the single-crystal structures show that the total solvent-accessible volumes are about 76.4% and 75.7% of the total crystal volumes for Zr-MOF-1 and Zr-MOF-2, respectively. The N_2 adsorption–desorption isotherms at 77 K and pore size distribution curves are shown in Figure S1 in the Supporting Information. The Brunauer–Emmett–Teller surface areas of Zr-MOF-1, Zr-MOF-2, and Zr-MOF-3 were calculated to be 1383, 1039, and 24 m^2 g^{-1}, respectively, verifying abundant active sites in highly crystalline Zr-MOF-1 and Zr-MOF-2 compared with the amorphous Zr-MOF-3. The total pore volumes of Zr-MOF-1, Zr-MOF-2, and Zr-MOF-3 are 0.589, 0.397, and 0.048 cm^3 g^{-1}, respectively. The pore size distributions of Zr-MOFs derived from the adsorption isotherms were analyzed by density functional theory (DFT) model, revealing a hierarchically porous structure of Zr-MOF-1 with micropores at 1.14, 1.41, 1.68 nm, and mesopores at 2.43 and 2.70 nm (Figure S1b, Supporting Information). Pore size distribution of Zr-MOF-2 shows a uniform micropore size at around 1.10 nm, which matches well with the crystal structure (Figure S1b, Supporting Information and Figure 1b). Guided by the single-crystal structures of these MOFs, powder X-ray diffraction (PXRD) patterns clearly show the phase purity of the synthesized MOFs (Figure S2, Supporting Information). The morphological features of these MOFs were studied by scanning electron microscopy (SEM). Zr-MOF-1 shows a cubic morphology with an average side length of 3.0 μm (Figure 1d), and Zr-MOF-2 presents a rod-like morphology with an average size of 6.0 × 1.5 × 1.5 μm^3 (Figure 1e). The Zr-MOF-3 (Figure 1c), which shows a blob-like morphology, is proved to possess an amorphous state by the PXRD (Figure S2, Supporting Information) and SEM (Figure 1f).[52] Compared to the ligand of H_4TTFTB, the insolubility of Zr-MOF-3 in *N*,*N*-dimethylformamide (DMF) shows the assembled state. Fourier transform infrared spectroscopy (FT-IR) characterizations were also conducted to study the coordination environment of amorphous Zr-MOF-3. In the FT-IR spectra of the ligands, Me-H_4TTFTB and H_4TTFTB, the strong peaks at 1692.5 and 1696.7 cm^{-1} correspond to the C=O stretching in the free COOH. For Zr-MOF-1, Zr-MOF-2, and Zr-MOF-3, the strong absorption peaks at 1598.0, 1601.6, and 1603.2 cm^{-1}, and the strongest peaks at 1419.3, 1418.1, and 1417.7 cm^{-1} originate from the coordinated COO^- groups (Figure S3, Supporting Information). Moreover, a small amount of free COOH in Zr-MOFs is revealed by the weak absorption band at 1967.6 cm^{-1} (Figure S3, Supporting Information).[53] Finally, through X-ray photoelectron spectroscopy (XPS) analysis and elemental mapping analysis, it can be found that amorphous Zr-MOF-3 is constituted of Zr, S, O, and C atoms (Figures S4 and S5, Supporting Information). The O 1s electron energy spectrum shows that there are three kinds of oxygen atoms in Zr-MOF-3 (Figure S6, Supporting Information). These three peaks at 530.0, 531.6, and 532.8 eV are assigned to the lattice oxygen, coordinated oxygen (COO^-), and chemisorbed oxygen (including hydroxyl group from COOH), respectively.[54]

Electrical and electrochemical properties of Zr-MOF-1, Zr-MOF-2, and Zr-MOF-3 with mass loading of 2.0 mg cm^{-2} were investigated. They all exhibit low electronic conductivity with the values of 1.15×10^{-7}, 5.65×10^{-8}, and 3.01×10^{-7} S cm^{-1}, respectively (Figures S7–S9, Supporting Information), in

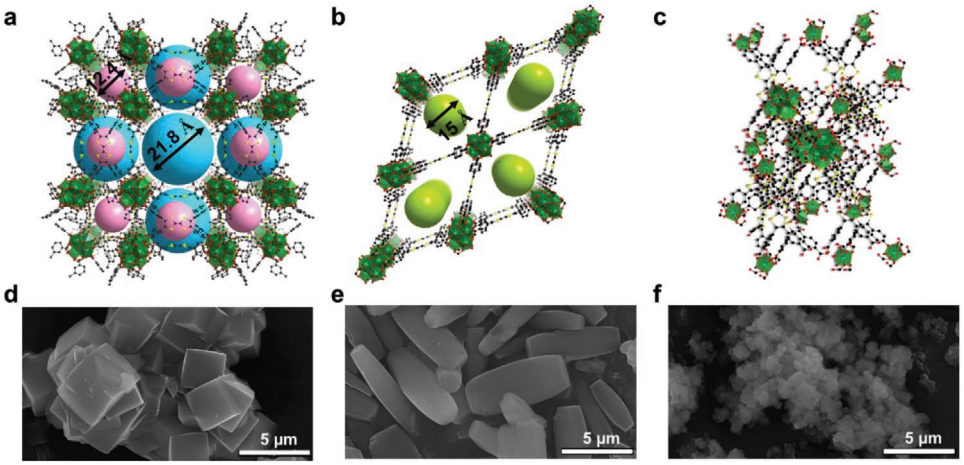

Figure 1. The single-crystal structures of a) hierarchical meso-microporous Zr-MOF-1 and b) microporous Zr-MOF-2, respectively. c) The schematic diagram of Zr-MOF-3 with amorphous structure. SEM images of the d) cubic Zr-MOF-1, e) rod-like Zr-MOF-2, and f) blob-like Zr-MOF-3, respectively. Scale bar, 5 μm.

ambient conditions. On the other hand, these materials show exceptional redox activity.[50] The inherent electrochemical performances of Zr-MOF||Li (Zr-MOF stands for all these three MOFs) half-cells were first studied. Cyclic voltammetry (CV) tests were conducted at a scan rate of 0.5 mV s^{-1} (**Figure 2**a). Notably, these two redox peaks of tetrathiafulvalene (TTF) units are in the range of 3.5–4.0 V versus Li/Li^+.[55] In this case, the broad anodic and cathodic peaks indicate the Li^+ insertion/extraction behaviors of Zr-MOF. The porous 3D frameworks with various microenvironments are beneficial to the insertion and transport of Li^+ ions. These microenvironments including benzene rings, carboxyl groups, uniformly distributed active sulfur sites of the TTF ligands, and the O/OH terminals of the Zr_6 inorganic clusters.[43,46,56–58] To assess the charge transport kinetics, the electrochemical impedance spectroscopy (EIS) measurements were performed at the frequency range of 10 mHz to 100 kHz. As depicted in Figure S10 in the Supporting Information, the EIS spectra are composed of a semicircle at high frequency and a linear part at low frequency. The equivalent circuit in Figure S10 in the Supporting Information is basically similar to that used for other anodes.[59,60] R_0 represents the internal resistance. The parallel circuit of R_{ct} and CPE1 represents charge transfer resistance and surface capacitance at the electrode surface, respectively. W_0 is connected in series to R_{ct} and describes Warburg diffusion impedance. In the R_s–CPE2 parallel circuit, R_s is the resistance for Li^+ ion conducting in the solid-electrolyte interphase (SEI) layer and CPE2 is the constant-phase elements for the SEI film. The similar semicircle at the high frequency suggests similar charge transfer impedances between the electrode materials and the electrolyte interface (≈50 Ohm). The sequential slopes at low frequency in order of Zr-MOF-1> Zr-MOF-2> Zr-MOF-3 imply the different diffusive kinetics of the electrolyte. Notably, Zr-MOF-1 shows the fastest Li ion transfer rate.

The galvanostatic charging–discharging curves of Zr-MOF anodes in Zr-MOF||Li half-cells at 100 mA g^{-1} (Figure 2b) exhibit sloping trends, verifying their pseudocapacitive properties. For clarity, the first cycle of the CV and galvanostatic charging–discharging curves of Zr-MOFs are presented in the Figures S11, S12, and S13 in the Supporting Information, showing the initial Coulombic efficiencies of 34.5% (Zr-MOF-1), 29.5% (Zr-MOF-2), and 24.0% (Zr-MOF-3), respectively. The specific capacities at the current densities from 100 to 2000 mA g^{-1} are shown in Figure 2c. The average values at 100 mA g^{-1} are 561, 434, and 374 mAh g^{-1} for Zr-MOF-1, Zr-MOF-2, and Zr-MOF-3, respectively. When the current density increases to 2000 mA g^{-1}, the discharge capacities are 108, 60, and 62 mAh g^{-1} for Zr-MOF-1, Zr-MOF-2, and Zr-MOF-3, respectively. Notably, the capacity of Zr-MOF-1 can be well recovered when the current density was reduced back to 100 mA g^{-1} (98.2%, 74.5%, and 66.0% for Zr-MOF-1, Zr-MOF-2, and Zr-MOF-3). To study the long-term cycling stability, the half-cells based on the Zr-MOFs anodes were cycled at the current density of 500 mA g^{-1} (Figure 2d). In the first ten cycles, the capacities of Zr-MOFs anodes dropped by 17.3%, 4.6%, and 5.5%, respectively. Accordingly, the Coulombic efficiencies reached to 99.9%, 99.6%, and 99.3% for Zr-MOF-1, Zr-MOF-2, and Zr-MOF-3, respectively. In the following 290 cycles, the specific capacity of these Zr-MOFs showed a little fluctuation. The capacity fluctuation during cycling is related to the dissolution/reformation of SEI film due to the large surface area and complex solid–liquid interfacial components of the anodes.[61,62] At last, the specific capacities of Zr-MOF-1 and Zr-MOF-2 show only a decrease of 5.5% and 2.2% in total, respectively, while Zr-MOF-3 shows the capacity increases of 15.0%. The enhancement of capacity may be attributed to the gradual electrochemical activation of the SEI film accompanied by better Li-diffusion kinetics.[63,64] Notably, the Coulombic efficiencies increased to ≈100% in the following 290 cycles, showing the formation of relatively stable SEI of Zr-MOFs anodes. Overall, the Zr-MOFs anodes show outstanding cycling stability with a capacity decay of only ≈0.06%, 0.01%, and –0.05% per cycle in the 300 cycles, for Zr-MOF-1, Zr-MOF-2, and Zr-MOF-3, respectively (Figure 2d). The structural stability of Zr-MOFs was also proved by the almost consistent PXRD patterns after the half-cell tests (Figure S14, Supporting Information). The slight changes in the peak intensity and location may attributed to certain framework flexibility, exposure of

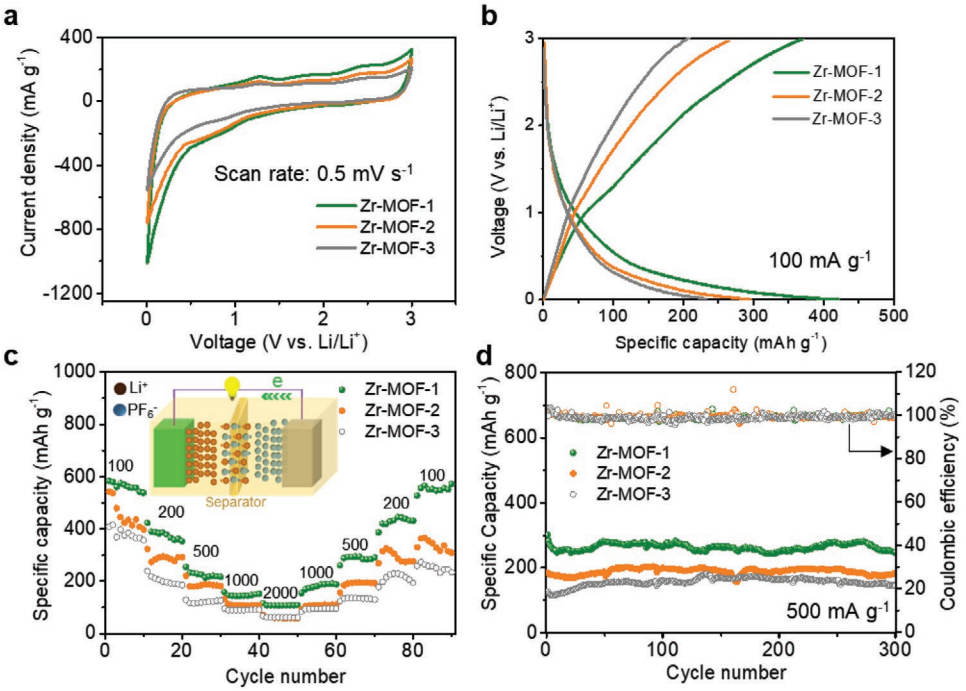

Figure 2. Electrochemical performance of Zr-MOF anodes. a) CV curves at a scan rate of 0.5 mV s^{-1}. b) The charging/discharging curves at the current density of 100 mA g^{-1}. c) Rate performances at different current densities from 100 to 2000 mA g^{-1}. The inset is the schematic illustration of half-cell device with Zr-MOF as the anode material and Li foil as the cathode material. d) Long-term cycling stability at the current density of 500 mA g^{-1}. The mass loadings of the active materials are 2.0 mg cm^{-2}.

different crystal faces, or the filling of the electrolyte.[50] Notably, the Zr-MOF-1 anode shows good long-term cycling stability at higher current densities of 1000 and 2000 mA g^{-1} (Figures S15 and S16, Supporting Information). The remarkable electrochemical performances of Zr-MOF-1 anode can be ascribed to the high crystallinity and the hierarchically ordered porosity derived from the well-organized 3D framework.[46,65] Comparing the half-cell performances of Zr-MOF-1 (420 mAh g^{-1}), Zr-MOF-2 (295 mAh g^{-1}), and Zr-MOF-3 (232 mAh g^{-1}), it can be concluded that the hierarchical meso-microporous channels and the high crystallinity are beneficial for the diffusion of Li ions (rapid Li^+ insertion/extraction). Considering the results of half-cell tests and the characteristic architectures, three points are addressed as following: 1) for the seeking of high stability, Zr-MOFs are recommended as electrodes; 2) improved porosity with suitable channels for the diffusion of Li^+ and holding of electrolyte are useful; 3) inclusion of redox active components in the framework is beneficial for the capacitive contribution. Furthermore, the incorporation of more active Li^+ interaction sites, redox active linkers, and conducting guests may further enhance the electrochemical performance of the MOF electrode.

To further understand the Li ion storage capability of Zr-MOF-1, CV measurements were conducted with the scan rates from 0.1 to 2.0 mV s^{-1} between 0.01 and 3.0 V versus Li/Li^+ (**Figure 3**a). According to the method described by Dunn group,[66] the CV results were utilized to investigate the electrochemical kinetic including the *b*-value (see Figure S17, Equations (S1) and (S 2) in the Supplementary Information) and the capacitance contribution to the overall capacity (see Figure S18, Equations (S3) and (S 4) in the Supplementary Information). The broad cathodic and anodic signals in all the scans indicate the Li^+ insertion/extraction reactions in the Zr-MOF-1‖Li cell. In Figure 3b, the *b*-values vary with charge/discharge state, suggesting different capacitive contributions during the lithiation/delithiation process. The *b*-value close to 1.0 signifies that the electrochemical process is controlled by capacitive response, while *b*-value close to 0.5 indicates the diffusion process is dominating. When inserting Li^+ ions in the Zr-MOF-1 anode, the *b*-value decreases from 0.92 (2.2 V vs Li/Li^+, open-circuit voltage) to 0.70 (0.4 V vs Li/Li^+), indicating the capacitive behavior dominates within this voltage range (discharge capacity of 140 mAh g^{-1} at 100 mA g^{-1}). The *b*-value then decreases to 0.57 (0.05 V vs Li/Li^+), indicating the electrochemical process turns into diffusion controlling (discharge capacity of 280 mAh g^{-1} at 100 mA g^{-1}). The electrochemical reaction below 0.4 V versus Li/Li^+ contributes to high capacity of Zr-MOF-1 but it hinders the high-rate capabilities. The *b*-values for the delithiation process are among 0.64 and 0.80, revealing the electrochemical process is related to both capacitive and diffusion behaviors. As shown in Figure 3c,d, the ratios of the calculated capacitive contribution are 24%, 29%, 39%, 48%, and 59% at the scan rates of 0.1, 0.2, 0.5, 1.0, and 2.0 mV s^{-1}, respectively. This result suggests that the electrochemical performance of Zr-MOF-1 electrode is simultaneously contributed by the capacitive behavior (accounts for the excellent rate capability) and the diffusion-controlled process (contributes to the high capacity). The further investigation on the improvement of the high-rate capabilities by finely tailoring the electrochemical and physicochemical properties of Zr-MOFs will be an important

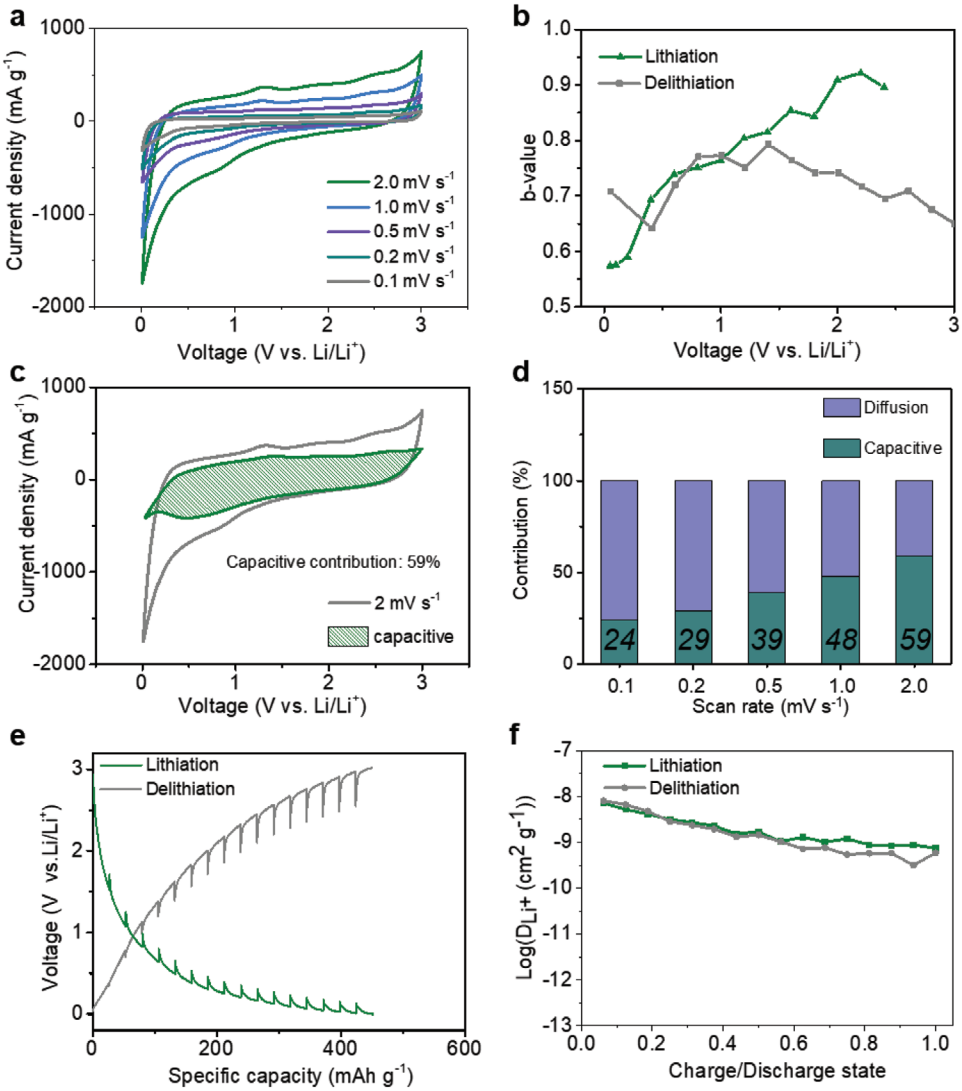

Figure 3. Electrochemical kinetics properties of Zr-MOF-1 anode. a) CV curves at various scan rates. b) Calculated *b*-values as a function of potential for lithiation and delithiation. c) CV curves at a scan rate of 2.0 mV s^{-1}. The part of capacitive contribution is marked by the green shaded region. d) Normalized contribution ratios of pseudocapacitive process to the total capacity at different scan rates. e) Potential response of Zr-MOF-1 anode during GITT measurement at a constant current density of 50 mA g^{-1}. f) The logarithm of calculated diffusion coefficients for lithiation and delithiation process.

aspect of our future research. We suggest that the capacitive contribution of the Zr-MOF anodes could be improved by tuning the particle size, modifying the functional groups, and constructing composites, such as in situ synthesis of conductive polymer in the pores. To investigate the diffusivity of active lithium species in Zr-MOF-1, the discharged and charged galvanostatic intermittent titration technique (GITT) curves of Zr-MOF-1 electrode are measured at the current density of 50 mA g^{-1} for 20 min followed by a rest time of 30 min to reach the steady-state voltage (Figure 3e).[67] As shown in Figure 3f, the Li ion diffusion coefficient (D_{Li}) (see Equation (S5) in the Supplementary Information) in the delithiation process is decreased from 8.0×10^{-9} to 5.4×10^{-10} cm^2 s^{-1} when the state of charge (SOC) increased from 0.06 to 0.75. The D_{Li} in the lithiation process decreased from 7.1×10^{-9} to 1.2×10^{-9} cm^2 s^{-1} when the SOC increased from 0.06 to 0.75. As the SOC increased from 0.75 to 1.0, the Li ion diffusivity nearly reached a relative stable level of 5.9–7.4 $\times$ 10^{-10} cm^2 s^{-1}. The Li^+ ion diffusion coefficients of Zr-MOF-2 and Zr-MOF-3 anodes are in the range of 3.76×10^{-10} to 3.52×10^{-12} cm^2 s^{-1} (Figure S19, Supporting Information) and 3.37×10^{-11} to 1.20×10^{-12} cm^2 s^{-1} (Figure S20, Supporting Information), respectively, which are an order magnitude smaller than Zr-MOF-1 anode. The faster Li^+ ion diffusion rate of Zr-MOF-1 proves that the hierarchically ordered porosity is conducive to the power output capability of electrodes. Generally, the Li ion diffusivity of Zr-MOF-1 is relatively high in the reported works.[67,68]

In order to have a clear idea of the lithiation and delithiation mechanisms in the Zr-MOF anodes, the attenuated total reflection–infrared spectroscopy (ATR–IR) was first conducted. The band at 1482.6 cm^{-1} derived from the C=C in the aromatic

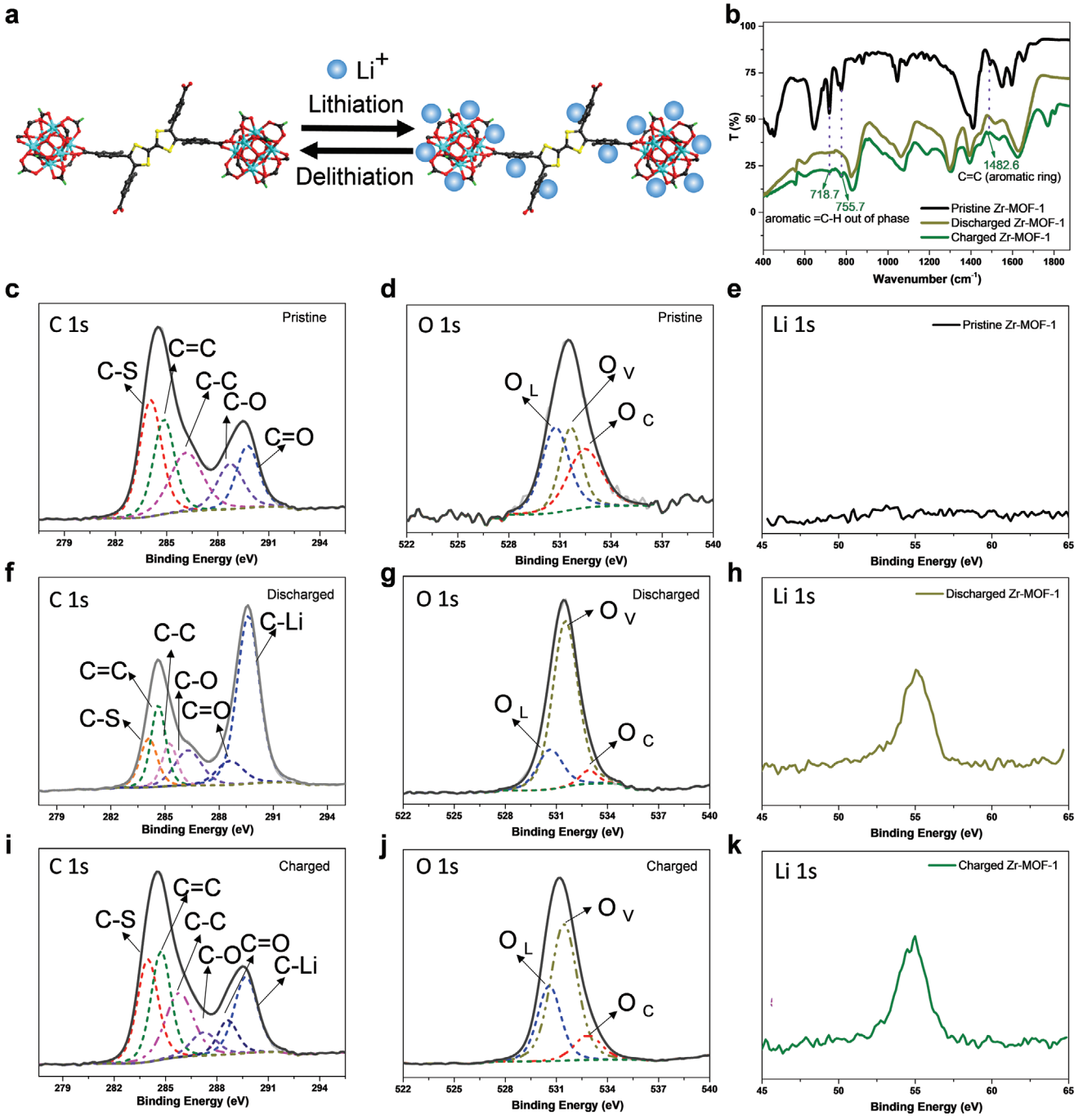

Figure 4. The ex situ characterization of the Zr-MOF-1 electrode. a) The proposed schemed lithiation and delithiation process in Zr-MOF-1 anode. b) The ATR–IR spectra of the pristine, discharged, and charged Zr-MOF-1 anode. The binding energy of c,f,i) Li 1s, d,g,j) C 1s, and e,h,k) O 1s of the pristine, discharged, and charged Zr-MOF-1.

ring disappeared in the discharge process compared to the pristine samples, while it recovered during the charge process (**Figure 4**b). Similar to the location at 718.7 and 755.7 cm^{-1} derived from the aromatic =C—H out of phase disappeared and recovered in the discharge process and the following charge process. These observations showed that the aromatic rings of the organic ligands have a strong interaction of Li^+ ions in the lithiation process. The XPS spectra of the pristine, charged, and discharged Zr-MOF-1 were further provided for more detailed information of the interaction between the Li^+ and the framework (Figure S21, Supporting Information and Figure 4c–k). First, the Li 1s clearly showed the interaction between the Li^+ and the framework in the charge and discharge process which is absent from the pristine samples. Second, the C 1s spectra clearly showed the existence of C—Li at 289.8 eV which is derived from the interaction of the carbon in aromatic ring and Li^+ ions.

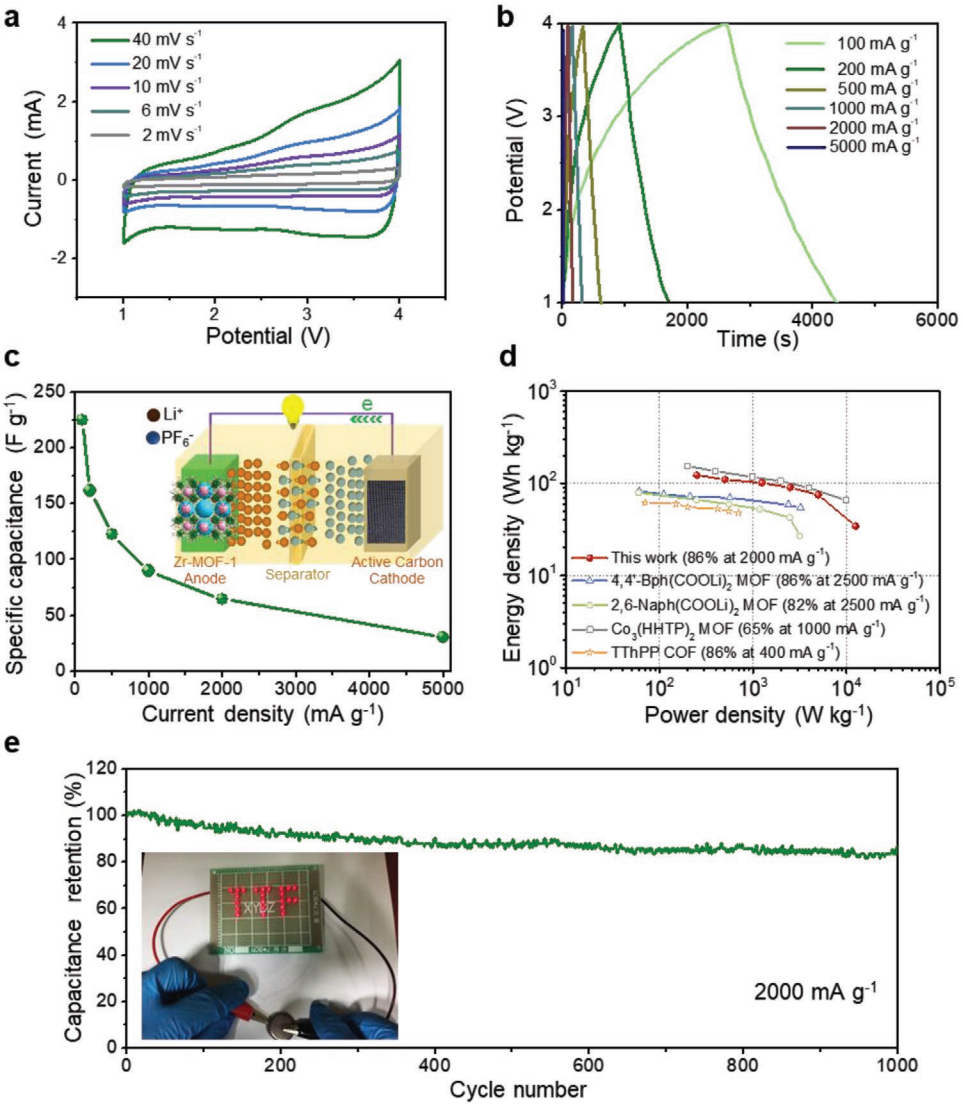

Figure 5. Electrochemical performances of HLICs with the Zr-MOF-1||AC configuration. a) CV curves of HLICs between 1.0 and 4.0 V at various scan rates from 2 to 40 mV s^{-1}. b) Charging–discharging curves of HLIC at different current densities from 100 to 5000 mA g^{-1}. c) Rate performances of HLIC at different current densities. The inset is the schematic illustration of HLIC with Zr-MOF-1 as anode material and AC as cathode material. d) Ragone plots of Zr-MOF-1||AC HLIC in this work and comparison with other reported HLICs involving pristine MOF/COF materials as anodes. e) Cycling performance at a current density of 2000 mA g^{-1}. The inset is an optical photograph showing a pattern of "TTF" consisting of 23 red LEDs simultaneously lighted by the Zr-MOF-1||AC HLIC.

The location of 284.0, 284.7, 285.8, 287.2, 288.6 eV are assigned to C—S, C=C, C—C, C—O, and C=O groups, respectively.[54,69] Third, the percentage enhancement of O 1s at 531.6 eV in the charge and discharge process showed the coordinated interaction between the O atoms and Li^+.[54] At last, the Zr 3d and S 2p peaks remain the same in different process excluded the possible active sites of Zr and S (Figure S22, Supporting Information). In all, the ATR–IR and XPS results together clarified the active site (including benzene rings, carboxyl groups, and the O/OH terminals of the Zr_6 inorganic clusters) in the framework (Figure 4a).

According to the outstanding electrochemical performances of Zr-MOF-1 electrode in the half-cell device, the equipped full-cell HLIC (inset in **Figure 5**c) with Zr-MOF-1||AC configuration was further studied. In the charging process, the electrolytic Li ions quickly insert into the channels of Zr-MOF-1 anode, while the PF_6^- ions were adsorbed onto/into the AC cathode in the meantime. The quasi-rectangular CV signals of Zr-MOF-1 electrode (Figure 5a) suggest the electrochemical kinetics balance of anode and cathode. Furthermore, the linear variation of galvanostatic charge/discharge profiles is slightly distorted (Figure 5b), confirming that the pseudocapacitance of Zr-MOF-1 anode is presented in the HLIC. Notably, the charge/discharge cycle can be accomplished within 20 s at the current density of 5000 mA g^{-1}, suggesting an outstanding rate capability. As shown in Figure 5c, the calculated specific capacitance (C_s) value (see Equations (6), (7) and (8) in Supplementary Information) reached to ≈225 F g^{-1} at 100 mA g^{-1}. The Ragone plots of the

Zr-MOF-1||AC HLIC in Figure 4d show a good balance between energy density and power density. The Zr-MOF-1||AC HLIC is able to achieve maximum energy density of 122.5 Wh kg^{-1} at the power density of 0.25 kW kg^{-1} and maximum power density of 12.5 kW kg^{-1} at the energy density of 34.4 Wh kg^{-1}, indicating the combination of synergetic advantages of LIBs and SCs (Figure 5d, see Equations (S9) and (S 10) in the Supplementary Information). The outstanding energy density, power density, and lifespan of the Zr-MOF-1||AC HLIC are competitive among the reported HLICs (Figure 5d and Tables S1 and S2, Supporting Information).[47–49,70] EIS curves are recorded for fresh HLIC and after cycling as shown in Figure S23 in the Supporting Information. The increased semicircle resistance after charging/discharging for 100 cycles may be attributed to the formation of SEI layer. Note that semicircle resistance keeps almost constant after 500 cycles, demonstrating limited growth of the SEI layer on the Zr-MOF-1 anode and fast Li^+ ion diffusion rate of Zr-MOF-1||AC HLIC. As a demonstration, a light panel of "TTF" constructed by 23 red light-emitting diodes (LEDs) was simultaneously powered by the Zr-MOF-1||AC HLIC (the inset of Figure 5e). The cycling stability of the HLIC was also evaluated by long-term cycling experiments (Figure 5e), showing a decant long-term cycling stability with ≈86% capacity retention after 1000 cycles at 2000 mA g^{-1}, which is also comparative among the reported HLICs.

3. Conclusion

In summary, we demonstrate the rational construction of redox-active Zr-MOF with tunable porosity and crystallinity as high-performance pseudocapacitive anode materials for HLICs. The Zr-MOFs exhibit remarkable electrochemical properties derived from the uniform distribution of active sulfur sites in the hierarchical porous nanochannels of MOF matrices, as well as the outstanding electrochemical redox activity and stability of the TTF-based linkers. The half-cell tests confirmed the distinct pseudocapacitive properties of Zr-MOF. Moreover, the HLIC properties and ion storage mechanism of Zr-MOFs are systematically studied. The as-prepared Zr-MOF-1||AC HLIC presented high energy density (up to 122.5 W h kg^{-1}), high power density (up to 12.5 kW kg^{-1}), and long cycling life within a wide operating voltage range (1.0–4.0 V), benefited from the favorable meso-microporous charge transport pathways and high crystallinity. This study may open a new avenue to broaden the direct application of MOFs for bridging the performance gap between batteries and supercapacitors.

4. Experimental Section

Chemicals: Anhydrous zirconium chloride ($ZrCl_4$, 98%), *N*-methyl-2-pyrrolidone (NMP), and benzoic acid were purchased from Aladdin. Anhydrous *N*,*N*-dimethylformamide (DMF), acetic acid, and lithium hexafluorophosphate ($LiPF_6$, 99.9%) were purchased from Nanjing chemical reagent Co., Ltd. All chemicals were used without further purification. H_4TTFTB and Me-H_4TTFTB (TTFTB = tetrathiafulvalene-tetrabenzoate) were prepared adopting the procedure reported in the previous work.[51]

Synthesis of Zr-MOF-1 $[Zr_6(Me\text{-}TTFTB)_{1.5}O_4(OH)_4(COO)_4]$: Briefly, Me-$H_4$TTFTB (0.250 g, 3.225 mmol), $ZrCl_4$ (0.750 g, 3.225 mmol), and benzoic acid (20 g, 163.667 mmol) were added into DMF (75 mL), followed by the addition of water (1.11 mL). The mixture was heated to 120 °C for 12 h in an oil bath, and then cooled down to room temperature. The orange-yellow cubic crystals (0.173 g) of Zr-MOF-1 were obtained by filtration and washed alternately with DMF and CH_3COCH_3 for three times, respectively. The yield was 25.9% (based on Me-H_4TTFTB).

Synthesis of Zr-MOF-2 $[Zr_6(TTFTB)_2O_8(OH_2)_8]$: Briefly, acetic acid (2.8 mL) was added into a mixture of H_4TTFTB (0.040 g, 0.060 mmol) and $ZrCl_4$ (0.040 g, 0.172 mmol) in DMF (8 mL). The mixture was capped and heated to 120 °C for 12 h, and then cooled to room temperature at a rate of 5 °C h^{-1}. Red microcrystals (0.046 g) of Zr-MOF-2 were obtained by filtration and washed alternately with DMF and acetone for three times. The yield was 75.0% (based on H_4TTFTB).

Synthesis of Amorphous State Zr-MOF-3: Briefly, H_4TTFTB (0.200 g, 2.58 mmol), $ZrCl_4$ (0.200 g, 0.86 mmol), and acetic acid (1.4 mL) were added into DMF (40 mL). The mixture was heated to 120 °C for 72 h in the oil bath, and then cooled to room temperature. Orange-yellow powder (0.058 g) of Zr-MOF-3 was obtained by filtration and washed alternately with DMF and acetone for three times.

Materials Characterizations: FT-IR spectra were recorded on Vector27 Bruker Spectrophotometer with KBr pellets in the 4000–400 cm^{-1} region. The PXRD patterns were collected with a scan rate of 0.1 s deg^{-1} on a Bruker Advance D8 diffractometer (40 kV, 40 mA) with Cu radiation (λ = 1.54056 Å) at room temperature. The SEM images were recorded on Hitachi S-3400N II equipped with an EX-250 energy-dispersive X-ray microanalyzer. XPS data were recorded on a PHI 5000 VersaProbe X-ray photoelectron spectrometer using standard monochromatic Al K_α radiation. The binding energies from the XPS spectra were calibrated against the C 1s peak located at 284.6 eV.

Electrochemical Characterizations: To prepare MOF electrodes, Zr-MOF-1, Zr-MOF-2, and Zr-MOF-3 powders were mixed with conductive carbon black additive (Ketjen Black) and polytetrafluoroethylene (PVDF) binder in *N*-methyl-2-pyrrolidone (NMP, 1 mL) with a mass ratio of 8:1:1, respectively. After stirring for 6 h, the homogenous slurry was coated on a Cu foil, dried under vacuum at 80 °C overnight, and then cut into circular disks (14 mm in diameter). The AC electrode was prepared on Al foil in the same way. The coin cells (CR2032 type) were assembled in an Ar-filled glove box where the moisture and oxygen concentrations were strictly limited to below 0.1 ppm. The electrolyte was 1.0 mol L^{-1} $LiPF_6$ in ethylene carbonate/dimethyl carbonate (EC/DMC, 1:1, v/v).

For the assembly of Zr-MOF||Li half-cells, Li foils were used as the counter electrode, and Celgard 2400 polypropylene membranes were used as the separators. The area mass loadings of MOF electrodes in half cells were 2.0 mg cm^{-2}.

For the assembly of Zr-MOF-1||AC HLICs, the MOF electrode was first pre-lithiated by adding 100 µL of electrolyte and then directly contacting with a piece of Li foil for 24 h in an Ar-filled glovebox. The AC electrode and the pre-lithiated MOF electrode were used as the cathode and anode in coin cells, respectively. In the HLIC, the area mass loadings of AC and MOF electrodes were 1.2 and 0.4 mg cm^{-2}, respectively.

CV measurements and EIS measurements were conducted on a Chenhua CHI-760E electrochemical workstation. The half-cells and HLICs were tested within the voltage range of 0.01–3.0 and 1.0–4.0 V, respectively. EIS measurements were carried out in the frequency range from 100 kHz to 0.01 Hz with the amplitude of 5 mV. The cycling and rate performances of the cells were measured on a LAND CT2001A analyzer at different current densities. The specific capacities were calculated according to the loading mass of active materials.

Calculation of b-Values: The contributions of capacitive-controlled and diffusion-controlled processes to the specific capacity were estimated by *b*-value in the following equations[71]

$$i = a\nu^b \tag{1}$$

$$\log i = b\log\nu + \log a \tag{2}$$

where i is the current response, ν is the scan rate, a and b are the adjustable parameters. The *b*-value could be determined by plotting

log*i* versus log*v*. If $b = 0.5$, it indicated a semi-infinite diffusion process controlled by Li^+ intercalation; while $b = 1$ suggested a capacitive behavior caused by surface redox reactions.[11] Therefore, for the active materials with apparent pseudocapacitive behavior, the peak current *i* varied linearly with the scan rate (*v*).

Calculation of Capacitive Contribution: To calculate the capacitive contribution, Equation (1) was transformed into the following equations[66]

$$i = k_1\nu + k_2\nu^{1/2} \tag{3}$$

$$i\,\nu^{-1/2} = k_1\nu^{1/2} + k_2 \tag{4}$$

where the current response *i* is equal to the sum of capacitive contribution ($k_1\nu$) and diffusion-controlled contribution ($k_2\nu^{1/2}$). The constants of k_1 and k_2 could be determined by plotting $i\nu^{-1/2}$ versus $\nu^{1/2}$. The $k_1\nu$ at different voltages was calculated and constituted the estimated capacitive contribution to the total current.

Calculation of Li^+ Ion Diffusion Coefficients: The GITT tests were performed at the current density of 50 mA g^{-1} for 20 min followed by a rest time of 30 min to reach the steady-state voltage. The Li^+ ion diffusion coefficient (D_{Li^+}) obtained from GITT was calculated according to the following equation[72]

$$D_{Li^+} = \frac{4}{\pi\tau}\left(\frac{mV}{MS}\right)^2\left(\frac{\Delta E_s}{\Delta E_t}\right)^2 = \frac{4}{\pi\tau}\left(\frac{m}{\rho S}\right)^2\left(\frac{\Delta E_s}{\Delta E_t}\right)^2 \tag{5}$$

where τ is the pulse time; *m*, *V*, *M*, and ρ are the mass loading, molar volume, molar mass, and density of the active materials, respectively; *S* is the surface area of the electrode; ΔE_s is the voltage difference between the steady state and the initial state of every step; ΔE_t is the voltage change during a pulse step excluding the iR drop. The densities of Zr-MOF-1 and Zr-MOF-2 were 0.58 and 0.59 g cm^{-3}, respectively, as measured by single-crystal XRD (SCXRD) analysis. The density of Zr-MOF-3 was 1.43 g cm^{-3}, which was calculated by measuring the mass and the volume of a pressed Zr-MOF-3 pellet.

Calculation of Cell-Discharge Capacitance (C_{cell}) and Specific Capacitance (C_s): The cell-discharge capacitance (C_{cell}) and the specific capacitance (C_s) of HLICs were calculated with the following equations[73]

$$\Delta V = (V_{max} + V_{min})/2 \tag{6}$$

$$C_{cell} = it/\Delta V \tag{7}$$

$$C_s = C_{cell}/m \tag{8}$$

where *i* is the applied current, *t* is the discharging time, ΔV is the voltage range, and *m* is the total mass of anode and cathode.

Calculation of Energy Density and Power Density: The energy density (*E*) and power density (*P*) were calculated according to the following equations

$$P = \Delta V \times I/m \tag{9}$$

$$E = P \times t \tag{10}$$

where *I* is the discharge current, *t* is the discharge time, *m* is the total loading mass of active materials in the AC cathodes and MOF anodes; V_{max} and V_{min} are the voltages at the beginning and the end of discharge steps.

Supporting Information

Supporting Information is available from the Wiley Online Library or from the author.

Acknowledgements

W.Y. and J.S. contributed equally to this work. This work was supported by the National Basic Research Program (nos. 2017YFA0208200, 2018YFA0306004), the National Natural Science Foundation of China (nos. 22022505, 21875099, 21872069, 51761135104), the Natural Science Foundation of Jiangsu Province (BK20180008), and the Fundamental Research Funds for the Central Universities of China (0205-14380219). The authors are grateful to Dr. Lei Sun in Argonne National Laboratory for his help on this work.

Conflict of Interest

The authors declare no conflict of interest.

Keywords

hierarchical porosity, hybrid lithium-ion capacitors, pseudocapacitive anode materials, zirconium metal–organic framework

Received: August 24, 2020
Revised: October 20, 2020
Published online:

[1] H. Wang, C. Zhu, D. Chao, Q. Yan, H. J. Fan, *Adv. Mater.* **2017**, *29*, 1702093.
[2] B. Y. Guan, A. Kushima, L. Yu, S. Li, J. Li, X. W. D. Lou, *Adv. Mater.* **2017**, *29*, 1605902.
[3] D.-G. Wang, Z. Liang, S. Gao, C. Qu, R. Zou, *Coord. Chem. Rev.* **2020**, *404*, 213093.
[4] V. Aravindan, J. Gnanaraj, Y. S. Lee, S. Madhavi, *Chem. Rev.* **2014**, *114*, 11619.
[5] A. Muzaffar, M. B. Ahamed, K. Deshmukh, J. Thirumalai, *Renewable Sustainable Energy Rev.* **2019**, *101*, 123.
[6] G. Zhu, T. Chen, L. Wang, L. Ma, Y. Hu, R. Chen, Y. Wang, C. Wang, W. Yan, Z. Tie, J. Liu, Z. Jin, *Energy Storage Mater.* **2018**, *14*, 246.
[7] Y. Ma, H. Chang, M. Zhang, Y. Chen, *Adv. Mater.* **2015**, *27*, 5296.
[8] C. Choi, D. S. Ashby, D. M. Butts, R. H. DeBlock, Q. Wei, J. Lau, B. Dunn, *Nat. Rev. Mater.* **2020**, *5*, 5.
[9] S. Trasatti, G. Buzzanca, *J. Electroanal. Chem. Interfacial Electrochem.* **1971**, *29*, A1.
[10] H. Y. Lee, J. B. Goodenough, *J. Solid State Chem.* **1999**, *144*, 220.
[11] V. Augustyn, J. Come, M. A. Lowe, J. W. Kim, P. L. Taberna, S. H. Tolbert, H. D. Abruna, P. Simon, B. Dunn, *Nat. Mater.* **2013**, *12*, 518.
[12] Y. Tang, Y. Zhang, O. I. Malyi, N. Bucher, H. Xia, S. Xi, Z. Zhu, Z. Lv, W. Li, J. Wei, M. Srinivasan, A. Borgna, M. Antonietti, Y. Du, X. Chen, *Adv. Mater.* **2018**, *30*, e1802200.
[13] Y. Berdichevsky, Y. H. Lo, *Adv. Mater.* **2006**, *18*, 122.
[14] H.-P. Cong, X.-C. Ren, P. Wang, S.-H. Yu, *Energy Environ. Sci.* **2013**, *6*, 1185.
[15] G. Cai, P. Darmawan, M. Cui, J. Wang, J. Chen, S. Magdassi, P. S. Lee, *Adv. Energy Mater.* **2016**, *6*, 1501882.
[16] C. K. Chiang, C. R. Fincher, Y. W. Park, A. J. Heeger, H. Shirakawa, E. J. Louis, S. C. Gau, A. G. MacDiarmid, *Phys. Rev. Lett.* **1977**, *39*, 1098.
[17] Y. Zhao, B. Liu, L. Pan, G. Yu, *Energy Environ. Sci.* **2013**, *6*, 2856.
[18] X. Cao, C. Tan, M. Sindoro, H. Zhang, *Chem. Soc. Rev.* **2017**, *46*, 2660.
[19] Y. Wang, Y. Song, Y. Xia, *Chem. Soc. Rev.* **2016**, *45*, 5925.

[20] O. M. Yaghi, *ACS Cent. Sci.* **2019**, *5*, 1295.
[21] O. M. Yaghi, M. J. Kalmutzki, C. S. Diercks, in *Introduction to Reticular Chemistry: Metal-Organic Frameworks and Covalent Organic Frameworks*, (Eds: O. M. Yaghi, M. J. Kalmutzki, C. S. Diercks), Wiley-VCH Verlag GmbH & Co. KGaA, Germany **2019**, pp. 1–27.
[22] Z. Chen, S. L. Hanna, L. R. Redfern, D. Alezi, T. Islamoglu, O. K. Farha, *Coord. Chem. Rev.* **2019**, *386*, 32.
[23] H. B. Wu, X. W. D. Lou, *Sci. Adv.* **2017**, *3*, eaap9252.
[24] F. Wang, X. Wu, X. Yuan, Z. Liu, Y. Zhang, L. Fu, Y. Zhu, Q. Zhou, Y. Wu, Y. W. Huang, *Chem. Soc. Rev.* **2017**, *46*, 6816.
[25] Y. Xu, Q. Li, H. Xue, H. Pang, *Coord. Chem. Rev.* **2018**, *376*, 292.
[26] H. Kaur, S. Sundriyal, S. K. Bhardwaj, S. Mishra, K.-H. Kim, A. Deep, *Coord. Chem. Rev.* **2018**, *369*, 15.
[27] Z. Liang, C. Qu, W. Guo, R. Zou, Q. Xu, *Adv. Mater.* **2018**, *30*, e1702891.
[28] D. Sheberla, J. C. Bachman, J. S. Elias, C. J. Sun, Y. Shao-Horn, M. Dinca, *Nat. Mater.* **2017**, *16*, 220.
[29] G. Givaja, P. Amo-Ochoa, C. J. Gomez-Garcia, F. Zamora, *Chem. Soc. Rev.* **2012**, *41*, 115.
[30] C. F. Leong, P. M. Usov, D. M. D'Alessandro, *MRS Bull.* **2016**, *41*, 858.
[31] L. Sun, M. G. Campbell, M. Dinca, *Angew. Chem., Int. Ed.* **2016**, *55*, 3566.
[32] Z. Zhang, H. Yoshikawa, K. Awaga, *J. Am. Chem. Soc.* **2014**, *136*, 16112.
[33] Z. Zhang, K. Awaga, *MRS Bull.* **2016**, *41*, 883.
[34] D. M. D'Alessandro, *Chem. Commun.* **2016**, *52*, 8957.
[35] A. Mallick, H. Liang, O. Shekhah, J. Jia, G. Mouchaham, A. Shkurenko, Y. Belmabkhout, H. N. Alshareef, M. Eddaoudi, *Chem. Commun.* **2020**, *56*, 1883.
[36] K. W. Nam, S. S. Park, R. Dos Reis, V. P. Dravid, H. Kim, C. A. Mirkin, J. F. Stoddart, *Nat. Commun.* **2019**, *10*, 4948.
[37] C. Yang, X. Li, L. Yu, X. Liu, J. Yang, M. Wei, *Chem. Commun.* **2020**, *56*, 1803.
[38] J. Su, W. He, X.-M. Li, L. Sun, H.-Y. Wang, Y.-Q. Lan, M. N. Ding, J.-L. Zuo, *Matter* **2020**, *2*, 711.
[39] T. Liu, Y. Li, *InfoMat* **2020**, *2*, 807.
[40] J. Pang, S. Yuan, J. Qin, M. Wu, C. T. Lollar, J. Li, N. Huang, B. Li, P. Zhang, H. Zhou, *J. Am. Chem. Soc.* **2018**, *140*, 12328.
[41] H. Jiang, X.-C. Liu, Y. Wu, Y. Shu, X. Gong, F.-S. Ke, H. Deng, *Angew. Chem.* **2018**, *130*, 3980.
[42] S. Yuan, L. Feng, K. Wang, J. Pang, M. Bosch, C. Lollar, Y. Sun, J. Qin, X. Yang, P. Zhang, Q. Wang, L. Zou, Y. Zhang, L. Zhang, Y. Fang, J. Li, H. C. Zhou, *Adv. Mater.* **2018**, *30*, e1704303.
[43] A. E. Baumann, X. Han, M. M. Butala, V. S. Thoi, *J. Am. Chem. Soc.* **2019**, *141*, 17891.
[44] K. M. Choi, H. M. Jeong, J. H. Park, Y. B. Zhang, J. K. Kang, O. M. Yaghi, *ACS Nano* **2014**, *8*, 7451.
[45] Q. Lin, X. Bu, A. Kong, C. Mao, X. Zhao, F. Bu, P. Feng, *J. Am. Chem. Soc.* **2015**, *137*, 2235.
[46] H. Jiang, X.-C. Liu, Y. Wu, Y. Shu, X. Gong, F.-S. Ke, H. Deng, *Angew. Chem., Int. Ed.* **2018**, *57*, 3916.
[47] Y. Ozawa, N. Ogihara, M. Hasegawa, O. Hiruta, N. Ohba, Y. Kishida, *Commun. Chem.* **2018**, *1*, 65.
[48] N. Ogihara, Y. Ozawa, O. Hiruta, *J. Mater. Chem. A* **2016**, *4*, 3398.
[49] J. Sun, L. Guo, X. Sun, J. Zhang, Y. Liu, L. Hou, C. Yuan, *J. Mater. Chem. A* **2019**, *7*, 24788.
[50] J. Su, S. Yuan, T. Wang, C. Lollar, J.-L. Zuo, J. Zhang, H.-C. Zhou, *Chem. Sci.* **2020**, *11*, 1918.
[51] J. Su, S. Yuan, H.-Y. Wang, L. Huang, J.-Y. Ge, E. Joseph, J. Qin, T. Cagin, J.-L. Zuo, H.-C. Zhou, *Nat. Commun.* **2017**, *8*, 2008.
[52] T. D. Bennett, A. K. Cheetham, *Acc. Chem. Res.* **2014**, *47*, 1555.
[53] I. Agirrezabal-Telleria, I. Luz, M. A. Ortuno, M. Oregui-Bengoechea, I. Gandarias, N. Lopez, M. A. Lail, M. Soukri, *Nat. Commun.* **2019**, *10*, 2076.
[54] L. Sun, R. Li, W. Zhan, Y. Yuan, X. Wang, X. Han, Y. Zhao, *Nat. Commun.* **2019**, *10*, 2270.
[55] H. Yang, Q. Wang, R. Zhang, B. D. Trimm, M. S. Whittingham, *Chem. Commun.* **2016**, *52*, 7580.
[56] J. Zhou, B. Wang, *Chem. Soc. Rev.* **2017**, *46*, 6927.
[57] J. Yang, P. Xiong, C. Zheng, H. Qiu, M. Wei, *J. Mater. Chem. A* **2014**, *2*, 16640.
[58] M. T. Li, N. Kong, Y. Q. Lan, Z. M. Su, *Dalton Trans.* **2018**, *47*, 4827.
[59] C. Wang, A. J. Appleby, F. E. Little, *J. Electroanal. Chem.* **2001**, *497*, 33.
[60] J.-S. Zheng, L. Zhang, A. Shellikeri, W. Cao, Q. Wu, J. P. Zheng, *Sci. Rep.* **2017**, *7*, 41910.
[61] I. T. Luca, E. Pollak, R. Kostecki, *Electrochem. Commun.* **2009**, *11*, 2157.
[62] Z.-S. Wu, W. Ren, L. Xu, F. Li, H.-M. Cheng, *ACS Nano* **2011**, *5*, 5463.
[63] W. Sun, X. Tang, Q. Yang, Y. Xu, F. Wu, S. Guo, Y. Zhang, M. Wu, Y. Wang, *Adv. Mater.* **2019**, *31*, 1903176.
[64] P. Xiao, F. Bu, R. Zhao, M. Aboud, I. Shakir, Y. Xu, *ACS Nano* **2018**, *12*, 3947.
[65] J. Zheng, J. Tian, D. Wu, M. Gu, W. Xu, C. Wang, F. Gao, M. H. Engelhard, J. G. Zhang, J. Liu, J. Xiao, *Nano Lett.* **2014**, *14*, 2345.
[66] J. Wang, J. Polleux, J. Lim, B. Dunn, *J. Phys. Chem. C* **2007**, *111*, 14925.
[67] X. Xue, R. Chen, C. Yan, P. Zhao, Y. Hu, W. Kong, H. Lin, L. Wang, Z. Jin, *Adv. Energy Mater.* **2019**, *9*, 1900145.
[68] K. Nakashima, T. Shimizu, Y. Kamakura, A. Hinokimoto, Y. Kitagawa, H. Yoshikawa, D. Tanaka, *Chem. Sci.* **2020**, *11*, 37.
[69] Z. Lei, Q. Yang, Y. Xu, S. Guo, W. Sun, H. Liu, L.-P. Lv, Y. Zhang, Y. Wang, *Nat. Commun.* **2018**, *9*, 576.
[70] H. Yang, S. Zhang, L. Han, Z. Zhang, Z. Xue, J. Gao, Y. Li, C. Huang, Y. Yi, H. Liu, Y. Li, *ACS Appl. Mater. Interfaces* **2016**, *8*, 5366.
[71] M. Sathiya, A. S. Prakash, K. Ramesha, J. M. Tarascon, A. K. Shukla, *J. Am. Chem. Soc.* **2011**, *133*, 16291.
[72] M. Tang, S. Zhu, Z. Liu, C. Jiang, Y. Wu, H. Li, B. Wang, E. Wang, J. Ma, C. Wang, *Chem* **2018**, *4*, 2600.
[73] J. H. Won, H. M. Jeong, J. K. Kang, *Adv. Energy Mater.* **2017**, *7*, 1601355.